IOP PUBLISHING PHYSICS IN MEDICINE AND BIOLOGY

Phys. Med. Biol. **53** (2008) 6947–6961 doi:10.1088/0031-9155/53/23/019

Non-iterative conductivity reconstruction algorithm using projected current density in MREIT

Hyun Soo Nam, Chunjae Park and Oh In Kwon

Department of Mathematics, Konkuk University, Korea

Received 2 May 2008, in final form 16 September 2008
Published 12 November 2008
Online at stacks.iop.org/PMB/53/6947

Abstract

Magnetic resonance electrical impedance tomography (MREIT) is to visualize the current density and the conductivity distribution in an electrical object Ω using the measured magnetic flux data by an MRI scanner. MREIT uses only one component B_z of the magnetic flux density $\mathbf{B} = (B_x, B_y, B_z)$ generated by an injected electrical current into the object. In this paper, we propose a fast and direct non-iterative algorithm to reconstruct the internal conductivity distribution in Ω with the measured B_z data. To develop the algorithm, we investigate the relation between the projected current density $\mathbf{J}^P$, a uniquely determined component of $\mathbf{J}$ by the map from current $\mathbf{J}$ to measured B_z data and the isotropic conductivity. Three-dimensional numerical simulations and phantom experiments are studied to show the feasibility of the proposed method by comparing with those using the conventional iterative harmonic B_z algorithm.

1. Introduction

The magnetic resonance current density imaging (MRCDI) technique has been proposed (Eyuboglu *et al* 1999, Gamba *et al* 1999, Joy *et al* 1989, Joy 2004, 1991, Scott *et al* 1992) by using a magnetic resonance imaging (MRI) scanner. The MRCDI measures the internal magnetic flux density $\mathbf{B} = (B_x, B_y, B_z)$ generated by an externally injected electrical current through the electrodes attached on the surface of an object Ω. Direct computations using Ampère's law $\mathbf{J} = \nabla \times \mathbf{B}/\mu_0$, where μ_0 is the magnetic permeability of the free space, produce the internal current density $\mathbf{J} = (J_x, J_y, J_z)$ corresponding to the measured magnetic flux density $\mathbf{B}$.

Since an MRI scanner measures only one component B_z of the magnetic flux density $\mathbf{B} = (B_x, B_y, B_z)$ where the main magnetic field direction is the z-direction, the imaging object should be rotated to measure all three components of $\mathbf{B}$ in the MRCDI. Indeed, a human body cannot be rotated in a conventional MRI scanner and even if it is possible, the rotation of the object may cause artifacts by misalignments of pixels and movements of internal organs. To overcome the rotating problem, it utilizes only one component B_z data to reconstruct the

conductivity and the current density in the object Ω recently. But MREIT requires at least two independent current injections to reconstruct the distinguishable conductivity distribution in Ω.

Most algorithms in MREIT are usually designed to extract some useful electrical information from the measured B_z data in the object Ω (Birgul *et al* 2006, Gao *et al* 2006, Hamamura *et al* 2006, Ider *et al* 1998, Joy 2004, Kwon *et al* 2002, Muftuler *et al* 2004, Park *et al* 2004b, Seo *et al* 2003).

Although imaging techniques in MREIT using B_z data have been rapidly developed and are at the stage of animal experiments nowadays, for practical usages of MREIT, it is important to develop a stable and fast algorithm to reconstruct the internal conductivity and current density in Ω.

Recently, the relations of $\mathbf{J}$ and B_z were analyzed using the map $\mathcal{T}$ from the current density vector field $\mathbf{J}$ to the measured B_z data in Park *et al* (2007). The projected current density $\mathbf{J}^P$ is provided by an orthogonal decomposition $\mathbf{J} = \mathbf{J}^P + \mathbf{J}^N$, where $\mathbf{J}^N$ belongs to the null space of the map $\mathcal{T}$, and $\mathbf{J}^P$ is in the orthogonal complement of the null space. The projected current density $\mathbf{J}^P$ is recovered directly by solving a two-dimensional harmonic equation from the measured B_z data.

To visualize the conductivity distribution using the measured B_z data, most developed algorithms need to solve tedious and time-consuming three-dimensional elliptic equations iteratively to update the conductivity because the conductivity and the current density information is concealed in the measured B_z data.

In this paper, we propose a fast and direct algorithm to reconstruct an isotropic conductivity distribution in Ω using the projected current $\mathbf{J}^P$ with two independent injected currents. The projected current $\mathbf{J}^P$ consists of the background current $\mathbf{J}^0$ and the curl of a potential which is a solution of a two-dimensional harmonic equation. By investigating relations between the projected current $\mathbf{J}^P$ and the conductivity distribution, the proposed algorithm directly extracts the conductivity information from the measured B_z data, resulting in the reconstruction of the internal conductivity in a real time with a background current.

The recovered conductivity image using the proposed method mainly depends how well the projected current $\mathbf{J}^P$ is recovered by the measured B_z data. The recovered projected current $\mathbf{J}^P$ is identical to the true current $\mathbf{J}$ when the z-component of J_z is similar to J_z^0; $\mathbf{J}^0$ is the background current, but there are some differences in a general three-dimensional current case. This means that the recovered conductivity also includes some gap comparing with the true conductivity for a general three-dimensional case. We also study about the stability between the recovered conductivity using $\mathbf{J}^P$ and the z-component $J_z - J_z^0$.

Three-dimensional numerical simulations were tested to validate the feasibility of the proposed algorithm, where the conductivity was designed to generate a three-dimensional current flow. To the case of the agarose gel phantom experiment, we compared the reconstructed conductivities using the proposed algorithm and the conventional harmonic B_z algorithm.

2. Theory

2.1. *Projected current density* $\mathbf{J}^P$ *of* $\mathbf{J}$

Let Ω be a three-dimensional, cylindrical and electrical conducting body with its boundary $\partial\Omega$. This domain can be expressed as the union of slices which are perpendicular to the z-axis:

$$\Omega = \bigcup_{t\in(-H,H)} \Omega_t, \qquad \text{where} \quad \Omega_t = \Omega \cap \{(x, y, z) \in \mathbb{R}^3 \mid z = t\}. \tag{1}$$

Let $\mathbf{n} = (n_1, n_2, n_3)$ be the outward unit normal vector on $\partial\Omega$. Electric current is injected in Ω through a pair of surface electrodes attached on $\partial\Omega$. The interior current density distribution $\mathbf{J} = (J_x, J_y, J_z)$ influenced by an injected current satisfies

$$\begin{aligned} \nabla \cdot \mathbf{J} &= 0 \qquad \text{in} \quad \Omega \\ \mathbf{J} \cdot \mathbf{n} &= g \qquad \text{on} \quad \partial\Omega. \end{aligned} \tag{2}$$

The concept of a projected current, $\mathbf{J}^P$, is introduced from the relations of $\mathbf{J}$ and measured B_z data since MREIT only measures one component magnetic flux density B_z. The projected current $\mathbf{J}^P$ is uniquely determined by the measured B_z data; it can be expressed as $\mathbf{J}^0 := \nabla\alpha$ and $\mathbf{J}^* := \left(\frac{\partial\beta}{\partial y}, -\frac{\partial\beta}{\partial x}, 0\right)$, where α is a homogeneous voltage potential satisfying

$$\begin{aligned} \nabla^2\alpha &= 0 \qquad \text{in} \quad \Omega \\ \nabla\alpha \cdot \mathbf{n} &= \mathbf{J} \cdot \mathbf{n} \qquad \text{on} \quad \partial\Omega \qquad \text{and} \qquad \int_{\partial\Omega} \alpha \, \mathrm{d}s = 0, \end{aligned} \tag{3}$$

and $\beta_t(x, y) := \beta(x, y, t)$ for $t \in (-H, H)$ satisfies the following two-dimensional Laplace equation for each slice $\Omega_t \subset \Omega$:

$$\begin{aligned} \tilde{\nabla}^2\beta_t &= \frac{1}{\mu_0}\nabla^2 B_z \qquad \text{in} \quad \Omega_t \\ \beta_t &= 0 \qquad \text{on} \quad \partial\Omega_t. \end{aligned} \tag{4}$$

For convenience, we use the notations $\nabla = \left(\frac{\partial}{\partial x}, \frac{\partial}{\partial y}, \frac{\partial}{\partial z}\right)$ and $\tilde{\nabla} = \left(\frac{\partial}{\partial x}, \frac{\partial}{\partial y}\right)$.

The recovered $\mathbf{J}^P$ is identical to the true current $\mathbf{J}$ if the z-components of $\mathbf{J}^P$ and $\mathbf{J}$ are same. As a special case, if the current $\mathbf{J}$ is transversal, then the true current $\mathbf{J}$ is completely recovered by solving (3) and (4). Although, for a general current $\mathbf{J} = (J_s, J_y, J_z)$, there exists some gap between the current $\mathbf{J}$ and the projected current $\mathbf{J}^P$, the difference stably depends on $J_z - J_z^0$:

$$\|\mathbf{J}^P - \mathbf{J}\| \leqslant C \left\{ \left\| J_z^0 - J_z \right\| + \left\| \frac{\partial J_z^0}{\partial z} - \frac{\partial J_z}{\partial z} \right\| \right\}, \tag{5}$$

where $\|\cdot\|$ is a usual L^2-norm in Ω. For more details, the concrete description is found in Park *et al* (2007).

2.2. *Relations between the current density* $\mathbf{J}$ *and the measured* B_z

For the determination of an isotropic conductivity in Ω, most algorithms have used at least two independent injected currents because infinitely many conductivities may generate the same interior current density (Kim *et al* 2003). By assuming that only one component magnetic flux density B_z is available without rotating the object; the conventional harmonic B_z algorithm uses the fundamental relation

$$-\frac{\partial J_y^1}{\partial x} + \frac{\partial J_x^1}{\partial y} = \frac{1}{\mu_0}\nabla^2 B_z^1 \qquad -\frac{\partial J_y^2}{\partial x} + \frac{\partial J_x^2}{\partial y} = \frac{1}{\mu_0}\nabla^2 B_z^2, \tag{6}$$

where $\mathbf{J}^i$ and B_z^i are the current densities and measured magnetic flux densities corresponding to the injection currents I^i, $i = 1, 2$. To characterize the relations between the current density $\mathbf{J}$ and the measured B_z, assume that the conductivity value is smooth in each segmented region D_k where $\Omega = \cup_{k=1}^M D_k$, σ belongs to a class,

$$\Sigma := \left\{ \sigma = 1 + \sum_{k=1}^{M} \mu_k \chi_{D_k} \,\middle|\, -1 < \mu_k < \infty, \mu_k \neq 0, \mu_k \text{ smooth in } D_k \right\}. \tag{7}$$

Here, χ_{D_k} denotes the characteristic function in D_k. For an isotropic conductivity σ, the current density can be represented as $\mathbf{J} = -\sigma\nabla u$ where the potential u is a solution of the following elliptic problem:

$$\begin{aligned} &\nabla\cdot(\sigma\nabla u) = 0 \qquad \text{in} \quad \Omega \\ &-\sigma\nabla u\cdot\mathbf{n} = \mathbf{J}\cdot\mathbf{n} \qquad \text{on} \quad \partial\Omega \qquad \text{and} \quad \int_{\partial\Omega} u\,\mathrm{d}s = 0. \end{aligned} \tag{8}$$

The current $\mathbf{J}$ and the measured B_z satisfy the relation

$$\nabla^2 B_z(\mathbf{r}) = 0 \text{ if and only if } \tilde{\nabla}\times(J_x, J_y) = -\tilde{\nabla}\sigma(\mathbf{r})\times\tilde{\nabla}u(\mathbf{r}) = 0. \tag{9}$$

In the region $\tilde{\nabla}\sigma \neq (0,0)$, $\nabla^2 B_z(\mathbf{r}) = 0$ means that $\tilde{\nabla}\sigma(\mathbf{r})$ is parallel to the vector $\tilde{\nabla}u(\mathbf{r})$. If we only use the relation $\tilde{\nabla}\times(J_x, J_y) = -\frac{1}{\mu_0}\nabla^2 B_z$ to reconstruct the conductivity image containing edge information, it is difficult to recover the edge of conductivity with one injection current and the corresponding measured B_z data. For these reasons, conventional conductivity reconstruction algorithms in MREIT using one component B_z data require at least two independent injection currents.

3. Methods

3.1. Reconstruction algorithm

We assume two independent projected currents:

$$\begin{aligned} \mathbf{J}^{i,P} &= \mathbf{J}^{i,0} + \mathbf{J}^{i,*} \\ &= \nabla\alpha_i + \left(\frac{\partial\beta_i}{\partial y}, -\frac{\partial\beta_i}{\partial x}, 0\right), \qquad i = 1, 2, \end{aligned} \tag{10}$$

where α_i and β_i are solutions of (3) and (4) corresponding to different injection currents, respectively. The projected currents $\mathbf{J}^{i,P}$ are identical to the true current $\mathbf{J}^i = -\sigma\nabla u_i$ if $\frac{\partial\alpha_i}{\partial z} = J_z^i$ and $\frac{\partial^2\alpha_i}{\partial z^2} = \frac{\partial J_z^i}{\partial z}$.

Generally, the currents $\mathbf{J}^i = -\sigma\nabla u_i$ satisfy the following relation:

$$\tilde{\nabla}\times\left(J_x^i, J_y^i\right) = -\tilde{\nabla}\sigma\times\tilde{\nabla}u_i = \frac{\tilde{\nabla}\sigma}{\sigma}\times\left(J_x^i, J_y^i\right) = \tilde{\nabla}\log\sigma\times\left(J_x^i, J_y^i\right) \tag{11}$$

for the two-dimensional curl operation $\tilde{\nabla}\times\left(J_x^i, J_y^i\right) := \frac{\partial J_y^i}{\partial x} - \frac{\partial J_x^i}{\partial y}$. Using the projected current $\mathbf{J}^{i,P} \approx \mathbf{J}^i = -\sigma\nabla u_i$, equation (6) and (11) yield

$$\tilde{\nabla}\log\sigma\times\left(J_x^{i,P}, J_y^{i,P}\right) \approx -\frac{1}{\mu_0}\nabla^2 B_z^i. \tag{12}$$

By setting $\tau := \log\sigma$, the vector $\tilde{\nabla}\tau$ in (11) can be represented with a usual normal basis $\mathbf{e}_1 = (1,0)$ and $\mathbf{e}_2 = (0,1)$ as

$$\tilde{\nabla}\tau = a(\mathbf{r})\mathbf{e}_1 + b(\mathbf{r})\mathbf{e}_2. \tag{13}$$

Relations (12) and (10) provide a matrix equation,

$$\mathbf{A}\mathbf{x} = (\mathbf{A_1} + \mathbf{A_2})\,\mathbf{x} = \mathbf{b}, \tag{14}$$

where

$$\mathbf{A_1} = \begin{pmatrix} \dfrac{\partial\alpha_1}{\partial y} & -\dfrac{\partial\alpha_1}{\partial x} \\ \dfrac{\partial\alpha_2}{\partial y} & -\dfrac{\partial\alpha_2}{\partial x} \end{pmatrix}, \qquad \mathbf{A_2} = \begin{pmatrix} -\dfrac{\partial\beta_1}{\partial x} & -\dfrac{\partial\beta_1}{\partial y} \\ -\dfrac{\partial\beta_2}{\partial x} & -\dfrac{\partial\beta_2}{\partial y} \end{pmatrix}, \tag{15}$$

$\mathbf{x} = (a(\mathbf{r}), b(\mathbf{r}))^T$ and $\mathbf{b} = (-\tilde{\nabla}^2\beta_1(\mathbf{r}), -\tilde{\nabla}^2\beta_2(\mathbf{r}))^T$. The transversal gradient vector $\tilde{\nabla}\tau$ for each imaging slice, Ω_t, is obtained by solving the matrix equation (14). The log-scale conductivity $\tau = \log\sigma$ is recovered from $\mathbf{x} = \left(\frac{\partial\tau}{\partial x}, \frac{\partial\tau}{\partial y}\right)$ in (14) by

$$\tau(\mathbf{r}) = -\int_{\Omega_t} \tilde{\nabla}\Phi_2(\mathbf{r}-\mathbf{r}')\cdot\tilde{\nabla}\tau(\mathbf{r}')\,\mathrm{d}\mathbf{r}' + \int_{\partial\Omega_t} \frac{\partial\Phi_2(\mathbf{r}-\mathbf{r}')}{\partial\nu}\tau(\mathbf{r}')\,\mathrm{d}l_{\mathbf{r}'}, \tag{16}$$

where Ω_t is the two-dimensional imaging plane $z = t$, and $\Phi_2(\mathbf{r}-\mathbf{r}') = \frac{1}{2\pi}\log|\mathbf{r}-\mathbf{r}'|$ is the two-dimensional fundamental solution of the Laplace equation. The value of τ on the boundary $\partial\Omega_t$ satisfies

$$\frac{\tau(\mathbf{r})}{2} + \frac{1}{2\pi}\int_{\partial\Omega_t} \frac{(\mathbf{r}-\mathbf{r}')\cdot\nu}{|\mathbf{r}-\mathbf{r}'|^2}\tau(\mathbf{r}')\,\mathrm{d}l'_{\mathbf{r}} = \frac{1}{2\pi}\int_{\Omega_t} \frac{(\mathbf{r}-\mathbf{r}')\cdot\tilde{\nabla}\tau(\mathbf{r}')}{|\mathbf{r}-\mathbf{r}'|^2}\,\mathrm{d}\mathbf{r}'. \tag{17}$$

Theoretically, the solvability of the integral equation (17) is well known, and we can compute τ in the imaging slice Ω_t using (16) (Oh *et al* 2003). The reconstructed τ provides the interior conductivity value $\sigma(\mathbf{r}) = \mathrm{e}^{\tau(\mathbf{r})}$. In practical situations using the measured noisy B_z data, since intensities of the current $\mathbf{J}$ are weak and noisy, and the measured B_z data are more distorted near the boundary $\partial\Omega_t$, it is difficult to expect a reliable reconstructed conductivity image near the boundary. For these reasons, regularizing terms added to reconstruct the conductivity distribution near the boundary.

With the homogeneous solution α_i, the proposed method recovers the interior conductivity distribution directly and rapidly without any iterative step because it only solves the two-dimensional Laplace equation (4) to image the conductivity distribution in the ROI region, instead of solving three-dimensional forward problems in Ω.

It is interesting to observe the role of stiff matrix $\mathbf{A_1} + \mathbf{A_2}$ in (14); the one component $\mathbf{A_1}$ from the homogeneous potentials α_i is the same with the stiff matrix of the first step of the harmonic B_z algorithm in Oh *et al* (2003), and the other component $\mathbf{A_2}$ from β_i in (4) has all contrast information of the conductivity. In other words, the conventional harmonic B_z algorithm updates iteratively the conductivity distribution in Ω by solving three-dimensional elliptic equations at each step to get the matrix component $\mathbf{A_2}$.

3.2. Sensitivity of the conductivity with respect to $\mathbf{J}^{i,P}$ *and* $\mathbf{J}^i$

We used the projected current $\mathbf{J}^{i,P}$ instead of $\mathbf{J}^i$ to extract conductivity information in (12). In this section, we investigate the influence of the approximated $\mathbf{J}^{i,P} \approx \mathbf{J}^i$ on the reconstructed conductivity distribution in Ω. To see more precisely, we denote τ^P as the reconstructed one from $\mathbf{J}^{i,P}$ and τ as the true one. From relation (11), we have

$$\tilde{\nabla}\tau \times \left(J_x^i, J_y^i\right) = \tilde{\nabla}\tau^P \times \left(J_x^{i,P}, J_y^{i,P}\right) \tag{18}$$

because the harmonic equation $\tilde{\nabla}^2\beta^i = \frac{1}{\mu_0}\nabla^2 B_z^i$ on the imaging slice Ω_t implies

$$\tilde{\nabla} \times \left(J_x^i, J_y^i\right) = \tilde{\nabla} \times \left(J_x^{i,P}, J_y^{i,P}\right) = -\frac{1}{\mu_0}\nabla^2 B_z^i. \tag{19}$$

By subtracting $\tilde{\nabla}\tau \times (J_x^i, J_y^i)$ from both sides of (18), the difference vector $\tilde{\nabla}(\tau^P - \tau)$ can be represented as a matrix form:

$$(\mathbf{A_1} + \mathbf{A_2})\,(\tilde{\nabla}\tau^P - \tilde{\nabla}\tau)^T = \mathbf{A_3}(\tilde{\nabla}\tau)^T, \tag{20}$$

where

$$\mathbf{A_3} = \begin{pmatrix} -\left(J_y^1 - J_y^{1,P}\right) & \left(J_x^1 - J_x^{1,P}\right) \\ -\left(J_y^2 - J_y^{2,P}\right) & \left(J_x^2 - J_x^{2,P}\right) \end{pmatrix}. \tag{21}$$

Equation (20) shows that the difference vector $\tilde{\nabla}(\tau^P - \tau)$ depends on the characteristics of $\mathbf{A_1} + \mathbf{A_2}$, $\mathbf{A_3}$ and $\tilde{\nabla}\tau$. We observe some notable features from (20); the determined τ^P converges to τ in a stable manner as $\mathbf{J}_i^P$ goes to $\mathbf{J}_i$ because the matrix $\mathbf{A_3}$ also vanishes. If the true conductivity σ is a constant on some imaging slice region, then the recovered conductivity from the projected current is also a constant because the difference $\tilde{\nabla}(\tau^P - \tau)$ is also vanishing by (20).

Using matrix equations (16) and (20), the difference between τ^P and τ can be represented as

$$\tau^P(\mathbf{r}) - \tau(\mathbf{r}) = -\int_{\Omega_t} \tilde{\nabla}\Phi_2(\mathbf{r} - \mathbf{r}') \cdot ((\mathbf{A_1} + \mathbf{A_2})^{-1}\mathbf{A_3}(\tilde{\nabla}\tau)^T)\, \mathrm{d}\mathbf{r}' + \int_{\partial\Omega_t} \frac{\partial\Phi_2(\mathbf{r} - \mathbf{r}')}{\partial\nu}(\tau^P(\mathbf{r}') - \tau(\mathbf{r}'))\, \mathrm{d}l_{\mathbf{r}'}. \tag{22}$$

From relation (22), the reconstructed conductivity $\sigma^P := \mathrm{e}^{\tau^P}$ from the projected current $\mathbf{J}^P$ has also stability depending on the z-components of $\mathbf{J}$ and $\mathbf{J}^P$:

$$\|\sigma^P - \sigma\| \leqslant C\left\{\left\|\frac{\partial\alpha}{\partial z} - J_z\right\| + \left\|\frac{\partial^2\alpha}{\partial z^2} - \frac{\partial J_z}{\partial z}\right\|\right\} \tag{23}$$

where the constant C depends on the condition number of $\mathbf{A_1} + \mathbf{A_2}$, $\tilde{\nabla}\tau$ and the variance of the boundary values $\tau^P - \tau$ on $\partial\Omega_t$.

3.3. Model of simulation

For a numerical simulation, we took a cylindrical phantom model with a diameter of 14 cm and a height of 20 cm as shown in figure 1(a). Two pairs of electrodes were attached at the surface of the model. The amount of each injection current was 10 mA compared with the conventional harmonic B_z algorithm. The target conductivity distribution σ had eight different anomalies with different conductivity values 2, 3, 0.2, 0.7 and background 1 as depicted in figure 1(b). If the simulated conductivity distribution is cylindrical, the projected current $\mathbf{J}^P$ is identical to the true current. To simulate a general case, we intentionally designed a three-dimensional conductivity shape and imaged at each slice of the model. Figure 1(c) shows the cross-sectional conductivity images of the model from the bottom to the top, 9 images were selected from total 24 slice images. The image (7) in figure 1(c) denotes the center slice image of the model.

3.4. Phantom experiments

For a phantom experiment, a current was injected into the imaging object through a pair of surface electrodes. The injection current produces an internal current density distribution that is determined by the geometry and conductivity distribution of the imaging object. We measured only the z-component of the induced magnetic flux density by using the ICNE MR pulse sequence which injects the current between the end of the first RF pulse and the end of the reading gradient (Park *et al* 2006). The phase-encoding gradient was switched on for a brief period T_{pe} before the signal was collected during the data acquisition time width T_s for a fixed echo time T_E. A cylindrical phantom with 12 cm diameter and height was attached two recessed electrodes at the middle of the phantom. We filled the background with saline solution (1 g/l CuSO4, 3.12 g/l NaCl) to control T_1 and T_2 decays of spin density. The conductivity value of the background was 0.6 S m $^{-1}$. Two cylindrical objects, the diameters of left and right anomalies were 3.6 cm and 3 cm, respectively, in figure 2(a) filled with an agar

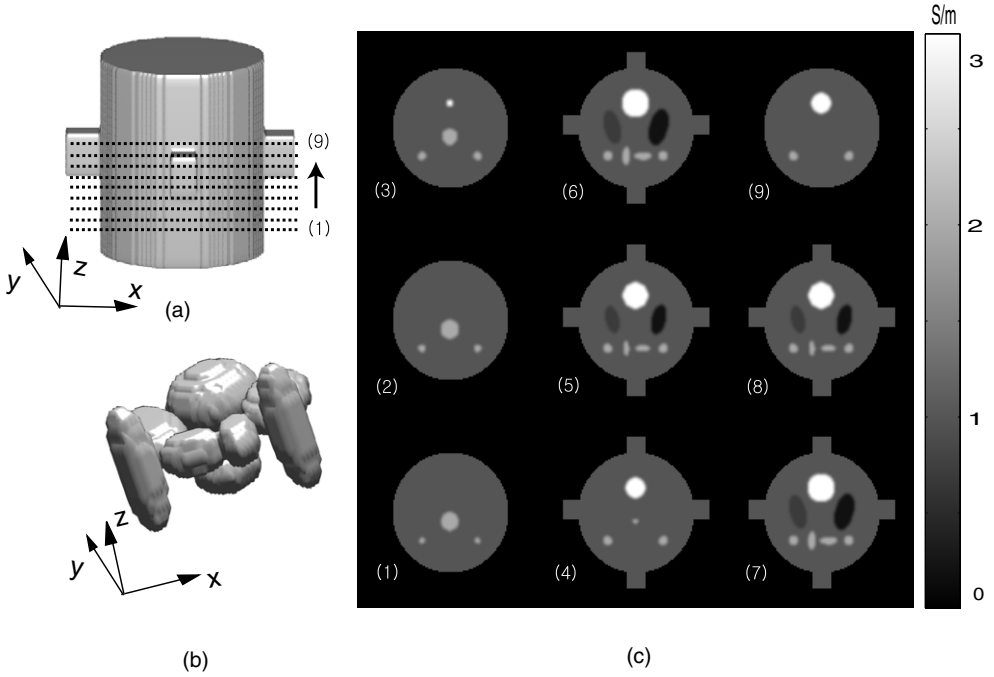

Figure 1. Simulation setup. (a) Three-dimensional cylindrical model and imaging slices. (b) Three-dimensional conductivity anomaly model. (c) Cross-sectional conductivity images at the imaging slices in (a).

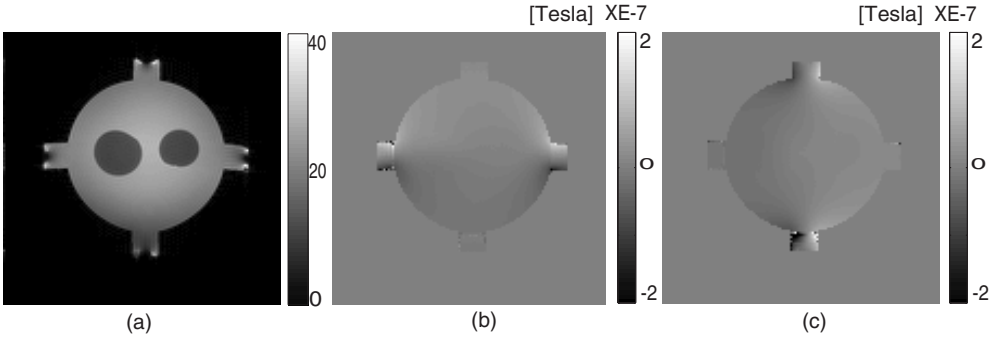

Figure 2. (a) MR magnitude image. (b) and (c) show images of measured B_z^i data due to transversal and vertical injection currents at the middle of the phantom.

gel (left : 1 g/l CuSO4, 12.5 g/l NaCl, 15 g/l agar, and right : 1 g/l CuSO4, 0.8 g/l NaCl, 15 g/l agar) to create a contrast in both conductivity and spin density, whose conductivity values of left one and right one are 1.4 and 0.3 S m $^{-1}$, respectively. The conductivity values were measured after the experiments using the four-electrode method with an impedance analyzer. Note that the MR magnitude images of two cylindrical objects in the agar phantom in figure 2(a) were almost same. After positioning the phantom inside a 3.0 T MRI scanner (Magnum 3, Medinus, Korea), we collected *k*-space MR data using the spin echo pulse sequence. The measured B_z data from the collected *k*-space data were shown in figures 2(b) and (c) due to transversal and vertical injection currents, respectively.

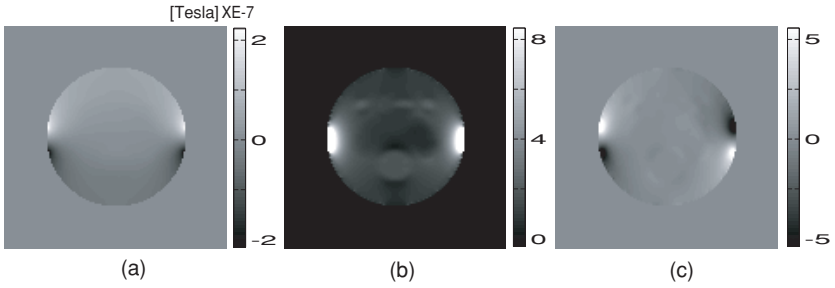

Figure 3. Simulated magnetic flux density and projected current density by injecting the x-direction current. (a) Simulated B_z data at the middle slice. (b) and (c) are the x- and y-components of the projected current $\mathbf{J}^{1,P} = (J_x^{1,P}, J_y^{1,P}, J_z^{1,P})$ for the simulation experiment.

Table 1. L^2-relative errors for the projected currents $E(J_x^{1,P})$, $E(J_y^{1,P})$ and $E(\mathbf{J}^{1,P})$ for each imaging slice (1)–(9) in figure 1(c).

Slice number	1	2	3	4	5	6	7	8	9
$E(J_x^{1,P})$	0.053	0.063	0.064	0.030	0.028	0.032	0.030	0.026	0.089
$E(J_y^{1,P})$	0.064	0.035	0.038	0.044	0.055	0.069	0.062	0.044	0.037
$E(\mathbf{J}^{1,P})$	0.050	0.055	0.055	0.036	0.034	0.036	0.033	0.031	0.077

We injected 10 mA current and used the total current injection time width $T_c + T_s = 24.6$ ms, $T_c = 15.1$ ms and data acquisition time width $T_s = 9.5$ ms for a fixed echo time $T_E = 25$ ms in the ICNE pulse sequence. The slice thickness was 6 mm with no slice gap, the number of axial slices was eight at the middle of the phantom, and $T_R/T_E = 800/25$ ms. Field of view (FOV) was 200×200 mm ^{2} with the matrix size 128×128, and the number of averaging was 4.

4. Results

4.1. Simulation results

We depicted the noiseless simulated B_z data due to the x-direction injected current using the three-dimensional MREIT solver (Lee *et al* 2003) at the middle slice of the model in figure 3(a) and the recovered projected current $\mathbf{J}^{1,P} = \mathbf{J}^{1,0} + \mathbf{J}^{1,*}$ in figures 3(b) and (c). The relative L^2-error of a reconstructed projected current density image is defined as

$$E\left(J_x^{1,P}\right) := \sqrt{\frac{\sum_{i,j}\left(J_x^1(i,j) - J_x^{1,P}(i,j)\right)^2}{\sum_{i,j}\left(J_x^1(i,j)\right)^2}} = \frac{\left\|J_x^1 - J_x^{1,P}\right\|}{\left\|J_x^1\right\|}. \tag{24}$$

Table 1 shows $E\left(J_x^{1,P}\right)$, $E\left(J_y^{1,P}\right)$ and $E(\mathbf{J}^{1,P})$ values for each imaging slice (1)–(9) in figure 1(c).

Figures 4(a) and (b) show the reconstructed conductivity images at each imaging slice by applying the harmonic B_z algorithm and the proposed algorithm using $\mathbf{J}^{i,P}$, $i = 1, 2$.

To obtain the conductivity images in figure 4(b), we only used the background potentials $u^{i,0}$ and the projected currents $\mathbf{J}^{i,P}$, $i = 1, 2$ by solving two-dimensional Laplace equations. Up to now, most iterative algorithms in MREIT including the harmonic B_z algorithm have to solve several tedious and time-consuming three-dimensional forward problems corresponding injection currents at each update step to arrive at the true conductivity image. Considering

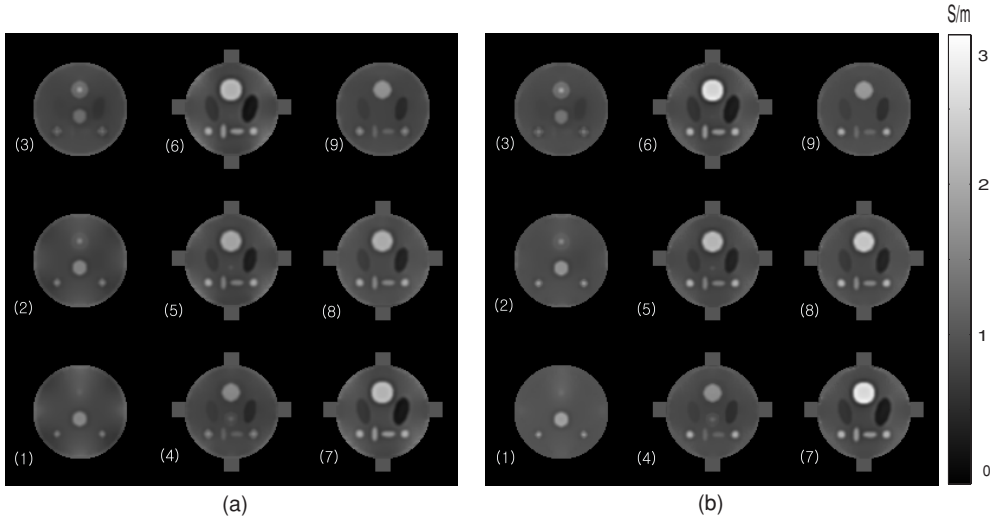

Figure 4. Simulation experiment results at each slice with noiseless B_z^i data, $i = 1, 2$. (a) The third updated conductivity images using the harmonic B_z algorithm. (b) Reconstructed conductivity images using the proposed projected current method.

the amounts of computation to visualize the conductivity distribution, those of the first updated conductivity image using the harmonic B_z algorithm are corresponding to those of the reconstructed one using the projected currents because both procedures commonly need to solve the 2×2 matrix system for each voxel and take a volume potential as in (16) starting from homogeneous potentials in Ω.

To visualize the conductivity in figure 4(a), we needed the conductivity updating step three times which requires three-dimensional forward solvers to update the voltage potentials. In spite of several updating steps, the reconstructed images of the harmonic method in figure 4(a) still had some loss in the region with high conductivity.

Simulation results at the center slice of image number (7) in figure 1(c) are displayed in figure 5. The profile images on the marked line in the target conductivity show that the value of the third updated conductivity using the harmonic B_z algorithm was lower than the reconstructed conductivity value using the projected current method.

The estimated relative L^2-error values $E(\sigma^r)$ on the centered slice for figures 5(b) and (c) were 0.212 and 0.1673, respectively.

The iterative harmonic B_z algorithm updates the conductivity distribution using the potentials corresponding to the previous updated conductivity. Since the updating ratio depends on the previous step conductivity values, thus it requires lots of iteration numbers to arrive at the high-conductivity values. Moreover, iteration numbers to arrive at the true conductivity depend on the anomaly shape and size and the conductivity value. With the noisy measured data, it is difficult to recover the high conductivity using the iterative algorithms without noise accumulation.

4.2. Recovery of conductivity using noised B_z data

We assume that the noise characteristics of the measured B_z follow the uniform Gaussian random variable with zero mean and variance $\mathrm{sd}^2(B_z)$. From the analysis by Sadleir *et al*

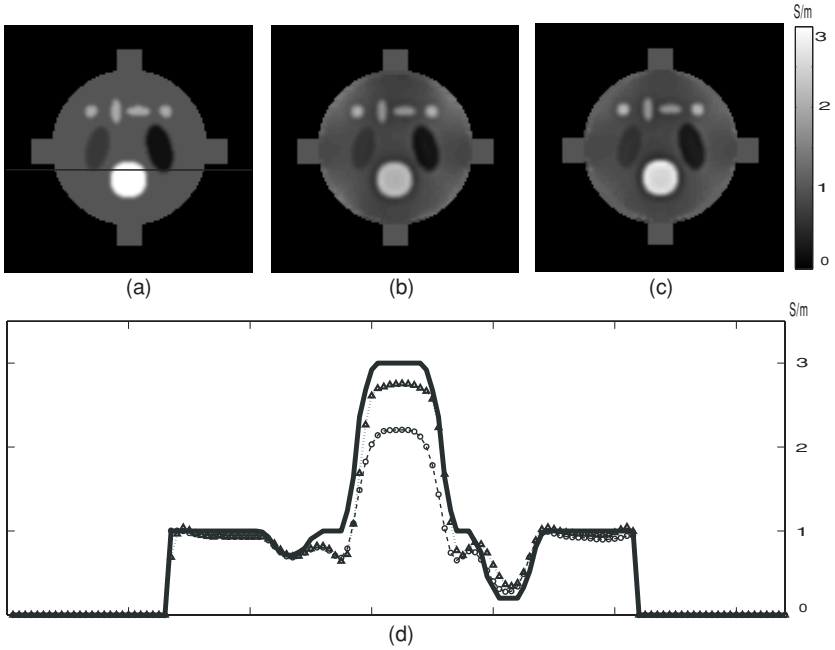

Figure 5. Simulation experiment results at the center of imaging model (the image of number (7) in figure 1(c)). (a) True conductivity image and a reference line. (b) The third updated conductivity images using the harmonic B_z algorithm. (c) Reconstructed conductivity image using the projected current method. (d) Profile images of the reconstructed conductivities on the marked line. Solid lines are used for the true conductivity; dashed line and triangle are for the projected current method; and dotted line and circ-mark are for third updated conductivity image of the harmonic B_z algorithm.

(2005) and Scott *et al* (1992), the noise standard deviation of B_z is described as

$$\mathrm{sd}(B_z)(\mathbf{r}) = \frac{1}{2\gamma T_c SNR(\mathbf{r})}, \tag{25}$$

and SNR is defined as

$$\mathrm{SNR}(\mathbf{r}) := \frac{|\mathcal{M}|(\mathbf{r})}{\mathrm{sd}(\mathcal{M})}, \tag{26}$$

where $\gamma = 26.75 \times 10^7$ is the gyromagnetic ratio of hydrogen, T_c is the current pulse width, and $\mathcal{M}$ is the measured spin density from an MRI scanner. We artificially added the Gaussian random noise in the simulated B_z^i data, $i = 1, 2$ to make SNR = 30, 50 and 100, respectively with $T_c = 20$ ms. Figures 6(a)–(c) show the reconstructed conductivity images using the projected current method. Figures 6(d)–(f) show the third updated conductivity images using the harmonic B_z algorithm. We represented the relative errors $E(\sigma_p^r)$, and $E(\sigma_{h,3}^r)$ for the projected current method, the third updated reconstructed conductivity distributions respectively at the middle slice in table 2. The noise levels of the reconstructed conductivity distribution in table 2 were higher than those of the projected currents because the recovery procedure depends on the condition numbers of the matrices $\mathbf{A_1}$, $\mathbf{A_2}$ and $\mathbf{A_3}$ in (20).

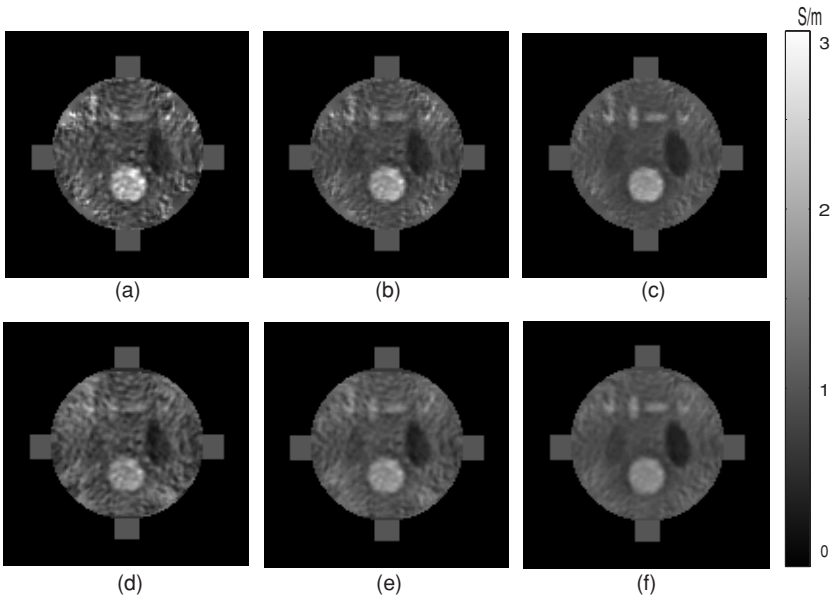

Figure 6. Simulation experiment results with noised B_z^i data; SNR = 30, 50, 100, respectively. (a)–(c) Reconstructed conductivity images using the projected current method. (d)–(f) Third updated conductivity images using the harmonic B_z algorithm.

Table 2. Relative errors $E(\sigma_p^r)$ for the projected current method, $E(\sigma_{h,3}^r)$ for the third updated reconstructed conductivity distributions, respectively.

	SNR = 30	SNR = 50	SNR = 100
$E(\sigma_p^r)$	0.3054	0.2789	0.2478
$E(\sigma_{h,3}^r)$	0.3177	0.2814	0.2717

4.3. Phantom experiment results

Figures 7(a) and (d) show the x- and y-components of $\mathbf{J}^{1,*} = \mathbf{J}^{1,P} - \mathbf{J}^{1,0}$ using the measured B_z^1 data. The recovered x- and y-components of the homogeneous and projected current are displayed in figures 7(b) and (e), and figures 7(c) and (f), respectively. Figures 8(a) and (b) are the recovered conductivity images using the harmonic B_z algorithm of the first and the fifth updated images. Because the computed projected current at the centered slice is almost same to the true current by injecting transversal currents, to include deviated regions, we displayed three recovered conductivity images from the center slice to the bottom region of the phantom among the measured eight slice B_z images with a thickness of 6 mm; the first row is the recovered conductivity images at the center slice, the middle and bottom rows are corresponding to 6 and 12 mm below slices from the centered one.

Figure 8(c) is the recovered conductivity image using the projected current $\mathbf{J}^{i,P}$, $i = 1, 2$. Although the projected currents may be slightly deviated from the true current, the directly recovered conductivity images at the middle and bottom rows using the projected current method showed closer conductivity values to the measured true values than results using the harmonic B_z algorithm.

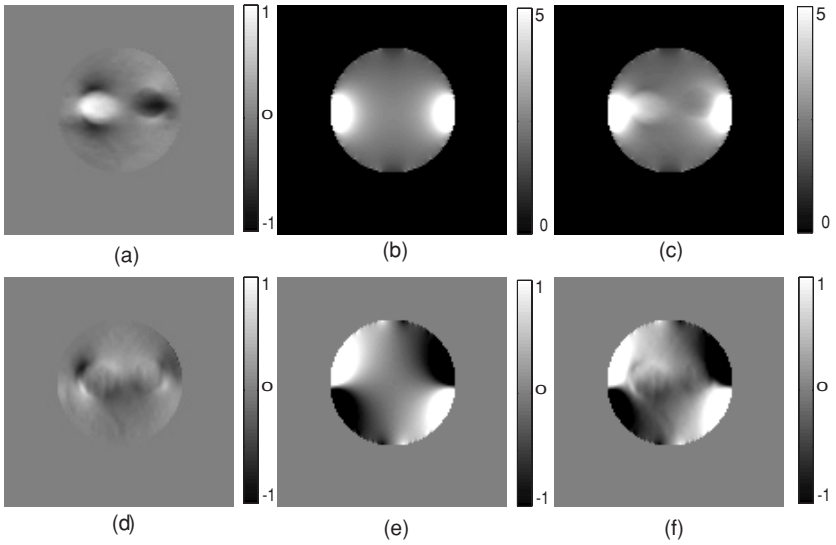

Figure 7. Projected current of the phantom experiment at the middle slice by a transversally injected current. (a) and (d) Components of $\mathbf{J}^{1,*} := (\frac{\partial \beta_1}{\partial y}, -\frac{\partial \beta_1}{\partial x}, 0)$ by solving (4). (b) and (e) The x- and y-components of the homogeneous current $\mathbf{J}^{1,0}$. (c) and (f) The x- and y-components of the recovered projected current $\mathbf{J}^{1,P}$.

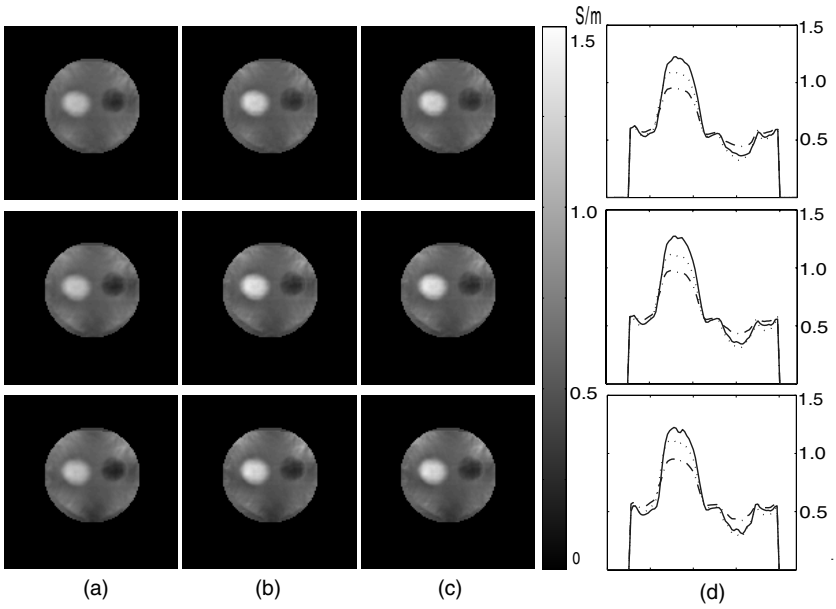

Figure 8. Phantom experiment results. (a) and (b) Recovered conductivity images using the harmonic B_z algorithm of first updated image and five times iterated image. (c) Recovered conductivity image using the projected current. (d) Profile images of the reconstructed conductivity on a line passing through the two included anomalies. Dashed-dot line, dot line and solid line are corresponding to the reconstructed conductivity (a), (b) and (c), respectively.

Note that the MR magnitude image did not distinguish the two cylindrical objects in figure 2, but clearly the conductivity image contrast was observed in two cylindrical anomalies in figure 8. The first updated conductivity from the homogeneous initial guess using the harmonic B_z algorithm provided the sufficient distinguishable contrast of the anomaly. The profile images in figure 8(d) compared the conductivity value on the line through the two included anomalies between the first and fifth updated images using the harmonic B_z method and the image using the proposed one. We required over 20 min to reconstruct the conductivity image figure 8(b) using the harmonic B_z method by iterating five times in pentium IV, CPU 2.4 GHz and 1 G ram operating system computing environment. However, we constructed the conductivity image within a minute using the projected currents in figure 8(c).

5. Discussion

The projected current $\mathbf{J}^P$ does not depend on the conductivity property; it can be calculated for the isotropic or anisotropic conductivity case. In this paper, under the assumption of the isotropic conductivity, we reconstructed the conductivity value directly and stably using the projected current $\mathbf{J}^P$.

For the harmonic B_z algorithm, let us denote the nth update stiff matrix:

$$\mathbf{A_n} = \begin{pmatrix} \dfrac{\partial u_n^1}{\partial y} & -\dfrac{\partial u_n^1}{\partial x} \\ \dfrac{\partial u_n^2}{\partial y} & -\dfrac{\partial u_n^2}{\partial x} \end{pmatrix}, \qquad \mathbf{b} = \frac{1}{\mu_0} \begin{pmatrix} \nabla^2 B_z^1 \\ \nabla^2 B_z^2 \end{pmatrix}. \tag{27}$$

The iteratively updated conductivity can be written in the following form :

$$\begin{aligned} \tilde{\nabla}\sigma_1 &= \tilde{\nabla}\sigma_0 + \mathbf{A}_0^{-1}(\mathbf{b} - \mathbf{A_0}\tilde{\nabla}\sigma_0) \\ \tilde{\nabla}\sigma_2 &= \tilde{\nabla}\sigma_0 + \mathbf{A}_0^{-1}(\mathbf{b} - \mathbf{A}_0\tilde{\nabla}\sigma_0) + \mathbf{A}_1^{-1}(\mathbf{b} - \mathbf{A}_1\tilde{\nabla}\sigma_1) \\ &\vdots \\ \nabla\tilde{\sigma}_{n+1} &= \tilde{\nabla}\sigma_0 + \textstyle\sum_{i=0}^{n}\left(\mathbf{A}_i^{-1}(\mathbf{b} - \mathbf{A}_i\tilde{\nabla}\sigma_i)\right) \\ &= \textstyle\sum_{i=0}^{n}\left(\mathbf{A}_i^{-1}\mathbf{b}\right) - \sum_{i=1}^{n}\tilde{\nabla}\sigma_i. \end{aligned} \tag{28}$$

The measured data $\mathbf{b}$ contain unavoidable noise $\mathbf{n}^T_{\nabla^2 B_z} := \left(n^1_{\nabla^2 B_z^1}, n^2_{\nabla^2 B_z^2}\right)$, $\mathbf{b} = \mathbf{b}^{\text{true}} + \mathbf{n}_{\nabla^2 B_z}$, where $\mathbf{b}^{\text{true}}$ is the noiseless data, and $\mathbf{n}_{\nabla^2 B_z}$ is the noise vector from the noise in the magnetic flux $B_z^i, i = 1, 2$. Relation (28) shows that the reconstructed $\tilde{\nabla}\sigma_{n+1}$ accumulates the noise effects $\sum_{i=0}^{n}\left(\mathbf{A}_i^{-1}\mathbf{n}_{\nabla^2 B_z}\right)$. Although the harmonic B_z algorithm includes the integration step to obtain σ^{n+1} from $\tilde{\nabla}\sigma_{n+1}$, the increasing iteration numbers to update the conductivity do not guarantee the improvement of the conductivity image.

The conductivity reconstruction procedure using the harmonic B_z and the proposed algorithms involves the integration of the gradient of conductivity for each slice. The conductivity values on the boundary at each imaging slice can be obtained by solving the boundary integral equation (17). However, since the gradient values of conductivity near the boundary include non-negligible noise, it is not easy to determine the conductivity values on the boundary using the boundary integral equation (17). In this paper, we simply used the known background conductivity values on the boundary to determine the interior conductivity value.

Comparing with the harmonic B_z algorithm, the proposed projected current based non-iterative method has provided stable and feasible reconstructed conductivity distributions. For

a general three-dimensional object, since the z-component of $\mathbf{J}^P$ is the z-component of the background current $\mathbf{J}^0$, the proposed method also has some gap between the reconstructed conductivity and the true one. However, the projected current $\mathbf{J}^P$ and the reconstructed conductivity using $\mathbf{J}^P$ have stabilities depending on the z-components of current J_z and J_z^P as shown in (5) and (23).

Since the z-component of $\mathbf{J}^P = \mathbf{J}^0 + \mathbf{J}^*$ is the z-component of the homogeneous current $\mathbf{J}^0$, we may expect that the current $\mathbf{J}^P$ can be closer to the true current $\mathbf{J}$ utilizing the assumption of the isotropic conductivity. In other hand, it may be useful to investigate the anisotropic conductivity property *via* the projected current $\mathbf{J}^P$.

6. Conclusions

To reconstruct conductivity images, many methods have been suggested but almost all of the algorithms use iterative methods and need heavy computations for solving three-dimensional forward problems to update. We proposed a new algorithm to reconstruct the conductivity using the projected current. The projected current is decomposed as the background current and the curl of the potential which is the solution of a simple two-dimensional harmonic equation. Using the projected current's structure and the measured magnetic flux density data efficiently, the proposed algorithm recovers the isotropic conductivity directly, stably and fast.

Acknowledgments

O Kwon was supported by the Korea Research Foundation Grant funded by the Korean Government (MOEHRD)(KRF-2005-201-C00004). This work was supported by the SRC/ERC program of MOST/KOSEF (R11-2002-103).

References

Birgul O, Hamamura M J, Muftuler L T and Nalcioglu O 2006 Contrast and spatial resolution in MREIT using low amplitude current *Phys. Med. Biol.* **51** 5035–50

Eyuboglu M, Reddy R and Leigh J S 1999 Imaging electrical current density using nuclear magnetic resonance *Elektrik* **6** 201–14

Gamba H R, Bayford D and Holder D 1999 Measurement of electrical current density distribution in a simple head phantom with magnetic resonance imaging *Phys. Med. Biol.* **44** 281–91

Gao N, Zhu S A and He B A 2006 New magnetic resonance electrical impedance tomography (MREIT) algorithm: the RSM-MREIT algorithm with applications to estimation of human head conductivity *Phys. Med. Biol.* **51** 3067–83

Hamamura M J, Muftuler L T, Birgul O and Nalcioglu O 2006 Measurement of ion diffusion using magnetic resonance electrical impedance tomography *Phys. Med. Biol.* **51** 2753–62

Ider Y Z and Birgul O 1998 Use of the magnetic field generated by the internal distribution of injected currents for electrical impedance tomography (MR-EIT) *Elektrik* **6** 215–25

Joy M L 2004 MR current density and conductivity imaging: the state of the art *Proc. 26th Ann. Int. Conf. IEEE EMBS* (California: San Francisco) pp 5315–9

Joy M L, Scott G C and Henkelman R M 1989 *In vivo* detection of applied electric currents by magnetic resonance imaging *Magn. Reson. Imaging* **7** 89–94

Kim Y J, Kwon O, Seo J K and Woo E J 2003 Uniqueness and convergence of conductivity image reconstruction in magnetic resonance electrical impedance tomography *Inverse Problems* **19** 1213–25

Kwon O, Woo E J, Yoon J R and Seo J K 2002 Magnetic resonance electrical impedance tomography (MREIT): simulation study of J-substitution algorithm *IEEE Trans. Biomed. Eng.* **48** 160–7

Lee B I, Oh S H, Woo E J, Lee S Y, Cho M H, Kwon O, Seo J K, Lee J Y and Baek W S 2003 Three-dimensional forward solver and its performance analysis in magnetic resonance electrical impedance tomography (MREIT) using recessed electrodes *Phys. Med. Biol.* **48** 1971–86

Muftuler L, Hamamura M, Birgul O and Nalcioglu O 2004 Resolution and contrast in magnetic resonance electrical impedance tomography(MREIT) and its application to cancer imaging *Technol. 3* 599–609

Oh S H, Lee B I, Woo E J, Lee S Y, Cho M H, Kwon O and Seo J K 2003 Conductivity and current density image reconstruction using harmonic B_z algorithm in magnetic resonance electrical impedance tomography *Phys. Med. Biol.* **48** 3101–16

Oh S H, Lee B I, Woo E J, Lee S Y, Kim T S, Kwon O and Seo J K 2005 Electrical conductivity images of biological tissue phantoms in MREIT *Physiol. Meas.* **26** 279–88

Park C, Kwon O, Woo E J and Seo J K 2004a Electrical conductivity imaging using gradient B_z decomposition algorithm in magnetic resonance electrical impedance tomography (MREIT) *IEEE Trans. Med. Imaging* **23** 388–94

Park C, Lee B I, Kwon O and Woo E J 2006 Measurement of induced magnetic flux density using injection current nonlinear encoding (ICNE) in MREIT *Physiol. Meas.* **28** 117–27

Park C, Lee B I and Kwon O 2007 Analysis of recoverable current from one component of magnetic flux density in MREIT *Phys. Med. Biol.* **52** 3001–13

Park C, Park E J, Woo E J, Kwon O and Seo J K 2004b Static conductivity imaging using variational gradient B_z algorithm in magnetic resonance electrical impedance tomography *Physiol. Meas.* **25** 269–75

Sadleir R *et al* 2005 Noise analysis in MREIT at 3 and 11 Tesla field strength *Physiol. Meas.* **26** 875–84

Scott G C, Joy M L, Armstrong R L and Henkelman R M 1991 Measurement of nonuniform current density by magnetic resonance *IEEE Trans. Med. Imaging* **10** 362–74

Scott G C, Joy M L, Armstrong R L and Hankelman R M 1992 Sensitivity of magnetic resonance current density imaging *J. Magn. Reson.* **97** 235–54

Seo J K, Yoon J R, Woo E J and Kwon O 2003 Reconstruction of conductivity and current density images using only one component of magnetic field measurements *IEEE Trans. Biomed. Eng.* **50** 1121–4